BIOPHYSICS

Single-molecule transport kinetics of a glutamate transporter homolog shows static disorder

Didar Ciftci[1,2], Gerard H. M. Huysmans[1], Xiaoyu Wang[1], Changhao He[1], Daniel Terry[1]*, Zhou Zhou[1], Gabriel Fitzgerald[1], Scott C. Blanchard[1,2]*†, Olga Boudker[1,2,3]†

Kinetic properties of membrane transporters are typically poorly defined because high-resolution functional assays analogous to single-channel recordings are lacking. Here, we measure single-molecule transport kinetics of a glutamate transporter homolog from *Pyrococcus horikoshii*, Glt_{Ph}, using fluorescently labeled periplasmic amino acid binding protein as a fluorescence resonance energy transfer–based sensor. We show that individual transporters can function at rates varying by at least two orders of magnitude that persist for multiple turnovers. A gain-of-function mutant shows increased population of the fast-acting transporters, leading to a 10-fold increase in the mean transport rate. These findings, which are broadly consistent with earlier single-molecule measurements of Glt_{Ph} conformational dynamics, suggest that Glt_{Ph} transport is defined by kinetically distinct populations that exhibit long-lasting "molecular memory."

INTRODUCTION

Secondary active transporters catalyze the uptake of solutes such as nutrients, neurotransmitters, and drugs across lipid bilayers (*1*). Their catalytic cycle begins with a transporter in a so-called outward-facing state, where it binds a substrate from the extracellular solution, followed by isomerization into an inward-facing state, the release of the substrate into the cytoplasm, and the return of the empty transporter into the outward-facing conformation (*1*). The rates of transport vary widely between transporters and are likely regulated by the rates of the conformational transitions. However, detailed kinetic studies of transporters have been limited due to the lack of high-resolution functional assays. Hence, a mechanistic understanding of transporters lags behind the ion channels, for which patch clamp and other single-channel electrophysiological recordings have provided a wealth of information over the last several decades (*2*–*4*). Here, we implement a single-transporter assay for a homolog of glutamate transporters, the sodium/aspartate symporter Glt_{Ph} (*5*), and establish parallels between the timing of its conformational transitions and transport events.

Glt_{Ph} is a well-studied model transporter, which operates by an "elevator" mechanism (*5*–*7*), in which distinct transport domains shuttle across the bilayer delivering the substrate L-aspartate (L-asp) and three coupled sodium (Na^+) ions from the extracellular to the intracellular side (fig. S1A) (*7*, *8*). Glt_{Ph} is a homotrimer with three peripherally located transport domains housed by a central scaffold or trimerization domain (fig. S1B). Previous studies of the transport domain dynamics conducted with single-molecule resolution showed that the domains moved independently of each other as well as a surprising degree of dynamic complexity (*9*–*12*). Specifically, only a fraction of the transporters was dynamic at a given time, while others remained largely quiescent (*9*–*11*). Infrequent transitions between nondynamic and dynamic modes were also observed in the wild-type (WT) transporter. Moreover, the observed transitions to quiescent periods were greatly reduced in a gain-of-function transport mutant R276S/M395R (termed RSMR for brevity) (*9*, *13*).

To detect individual transport events, we developed a fluorescence resonance energy transfer (FRET)–based sensor using aspartate/glutamate–binding periplasmic protein PEB1a (*14*). Periplasmic binding proteins have been used for FRET-based sensor design (*15*) because they share a common "clamshell" architecture and binding mechanism (*15*) where they transition from an open to a closed conformation upon ligand binding (Fig. 1A). We encapsulated fluorescently labeled PEB1a in proteoliposomes harboring single Glt_{Ph} transporters and recorded time-dependent FRET efficiency changes reflecting transport activity using total internal reflection fluorescence (TIRF) (*16*, *17*) microscopy with single-molecule resolution (smFRET) similarly to a recently reported assay for a neutral amino acid transporter (*18*). From these recordings, we extracted the timing of the first transport event and the consecutive transport turnover rates. Notably, individual Glt_{Ph} transporters showed transport rates ranging from a few to hundreds of seconds per cycle. The timing of the transport events was consistent with the timing of the transport domain dynamics (*9*, *10*) in both WT Glt_{Ph} and the RSMR mutant, in which the latter showed an increased fraction of the fast-working transporters. Both single-molecule conformational dynamics and transport assays suggest that the transporters sample multiple dynamic modes that persist for periods substantially longer than the catalytic turnover times. This so-called static rate disorder is reminiscent of phenomena previously observed in enzymes and channels (*19*–*24*).

RESULTS

Engineering of L-asp sensor

We introduced two cysteine mutations, N73C and K149C, into a cysteine-less version of PEB1a at positions where we expected a substantial decrease in interresidue distance upon L-asp binding (fig. S2A). The double cysteine mutant of PEB1a (ccPEB1a for brevity) showed specific, high-efficiency labeling with LD555p and LD655 dyes, self-healing fluorophores based on Cy3 and Cy5, respectively (fig. S2B) (*25*). After extensive dialysis to remove bound ligands, fluorescently labeled PEB1a was immobilized in passivated quartz microfluidics chambers and imaged using smFRET TIRF microscopy at a 10-s^{-1} frame rate. Individual molecules yielded smFRET trajectories with

[1]Department of Physiology and Biophysics, Weill Cornell Medicine, 1300 York Avenue, New York, NY 10065, USA. [2]Tri-Institutional Training Program in Chemical Biology, New York, NY 10065, USA. [3]Howard Hughes Medical Institute, Weill Cornell Medicine, New York, NY, 10065, USA.
*Present address: Department of Structural Biology, St. Jude Children's Research Hospital, Memphis, TN 38105-3678, USA.
†Corresponding author. Email: olb2003@med.cornell.edu (O.B.); scott.blanchard@stjude.org (S.C.B.)

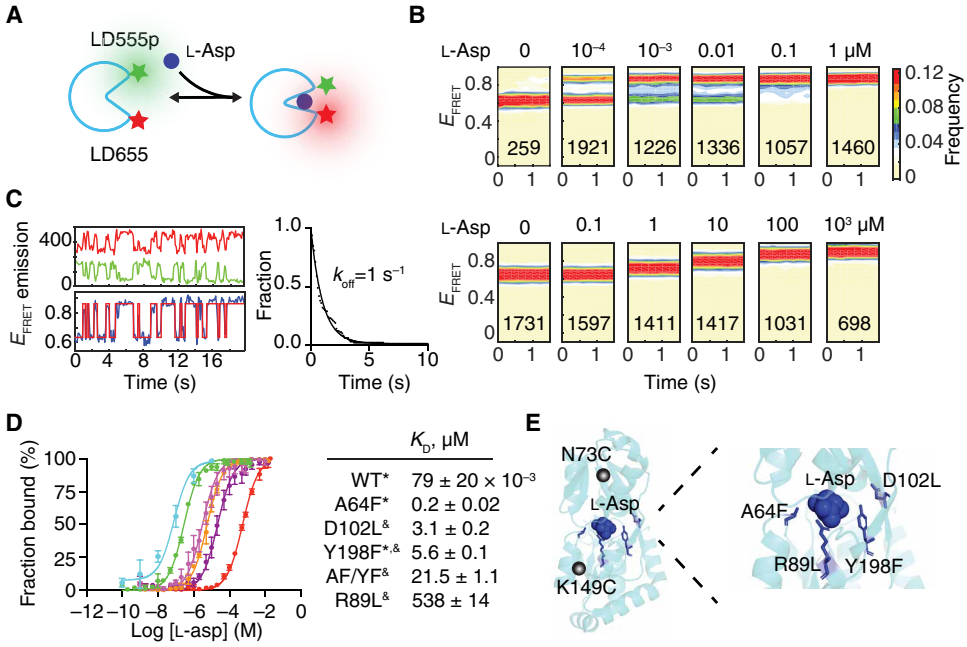

Fig. 1. smFRET sensor of L-asp based on PEB1a. (**A**) Clamshell L-asp binding mechanism of PEB1a and FRET-based detection. (**B**) Population contour plots of ccPEB1a (top) and ccPEB1a-Y198F (bottom). Here and elsewhere, the numbers on the panels correspond to the number of molecules used to construct the plots; the scale bar for this and other contour plots is to the right. (**C**) A single molecule recording of ccPEB1a. Shown are fluorescence emissions from LD555p (green) and LD655 (red) dyes (top) and FRET efficiency (blue) with idealization (red) using a three-state model (bottom). At right, dwell times in the 0.87 FRET (bound) state of ccPEB1a are shown as a survival plot (symbols) and fitted to an exponential decay function (solid line). (**D**) Binding isotherms of ccPEB1a (blue) and the mutants: A64F (green), D102L (magenta), Y198F (orange), Y198F/A64F (AF/YF, purple), and R89L (red). Solid lines are fits to one-site binding equations. Data are means and SEs from three independent experiments. Fitted K_d values are shown on the right. Binding was measured by smFRET (*) or bulk fluorimetry (&). (**E**) Cartoon representation of ccPEB1a with the binding site expanded. L-asp and mutated residues are shown as sticks.

constant efficiency of 0.65 ± 0.05 in the absence of L-asp and 0.87 ± 0.03 when 1 μM L-asp was added (Fig. 1B). At intermediate L-asp concentrations, we observed transitions between discrete lower- and higher-FRET efficiency states corresponding to binding and unbinding events (Fig. 1C). Plotting mean FRET efficiency as a function of L-asp concentration yielded a binding isotherm consistent with 79 ± 20 nM dissociation constant, K_d (Fig. 1D). On the basis of the dwell times of the high-FRET state at 1 nM L-asp, we estimated the binding and unbinding rates to be ~0.13×10^8 s^{-1} M^{-1} and 1 s^{-1}, respectively (Fig. 1C). We further generated ccPEB1a variants with reduced affinity for L-asp by mutating residues around the binding site (Fig. 1, D and E). ccPEB1a-Y198F variant yielded smFRET trajectories with constant efficiency of 0.63 ± 0.01 in the absence of L-asp and 0.86 ± 0.01 when 100 μM L-asp was added. Notably, the K_d's measured by bulk fluorimetry and by smFRET for ccPEB1a-Y198F mutant agreed well, yielding K_d's of 5.6 ± 1 and 3.6 ± 0.4 μM, respectively, which we attribute to an increased dissociation rate. Consistent with this idea, we did not detect discrete transitions between the low- and high-FRET efficiency states in smFRET trajectories of Y198F and other mutants obtained at L-asp concentrations near their K_d values. Instead, we observed intermediate FRET values suggesting that binding and unbinding events occurred at a time scale that was faster than the imaging rate (Fig. 1B and fig. S2D).

Single-molecule transport assay

For transport assays, we used cysteine-less variants of Glt_{Ph} and of the RSMR mutant harboring a single cysteine mutation N378C on the extracellular side of the transporter (termed WT and RSMR for brevity) (*9*, *10*). Cys378 has been previously used to fluorescently label and to surface immobilize Glt_{Ph} with high efficiency and specificity (*9*, *10*). Glt_{Ph} variants were reconstituted into 100-nm liposomes at low protein-to-lipid ratio (PLR) of 1:1000 (w/w), corresponding to ~5.4 trimers per 10^6 lipids, aiming to enrich for vesicle populations with no more than one transporter trimer. To establish the reconstitution stoichiometry, we labeled WT Glt_{Ph} with LD555p dye before reconstitution, immobilized the proteoliposomes in smFRET chambers via biotin-phosphatidylethanolamine (biotin-PE), and counted the number of photobleaching events per vesicle. We expect ~60% of liposomes to contain no transporters based on Poisson statistics. Of those that did contain a transporter, we found that ~70% had one trimer, while the remainder had two or more (fig. S3, A and B). For transport measurements, we reconstituted the WT and RSMR Glt_{Ph} proteins derivatized with biotin-PEG_{11}-maleimide at the same PLR of 1:1000 into liposomes containing no biotin-PE. We encapsulated LD555p/LD655-labeled ccPEB1a-Y198F mutant using freeze/thaw cycles followed by extrusion and surface-immobilized proteoliposomes via biotinylated transporters (Fig. 2A) (*9*). Photobleaching experiments confirmed that nearly all vesicles containing sensors had only one (fig. S3, C and D). Notably, our immobilization strategy used for transport measurements selects for the liposomes containing the transporters with their extracellular side facing vesicle exterior. Empty liposomes or those containing the transporter in the opposite orientation are washed away, except for a small fraction of those that attach nonspecifically.

Among the smFRET trajectories recorded for the proteoliposomes, 62 ± 7% showed initial FRET efficiency between 0.4 and 0.7 with a mean value of 0.63 ± 0.01, as expected for the ligand-free

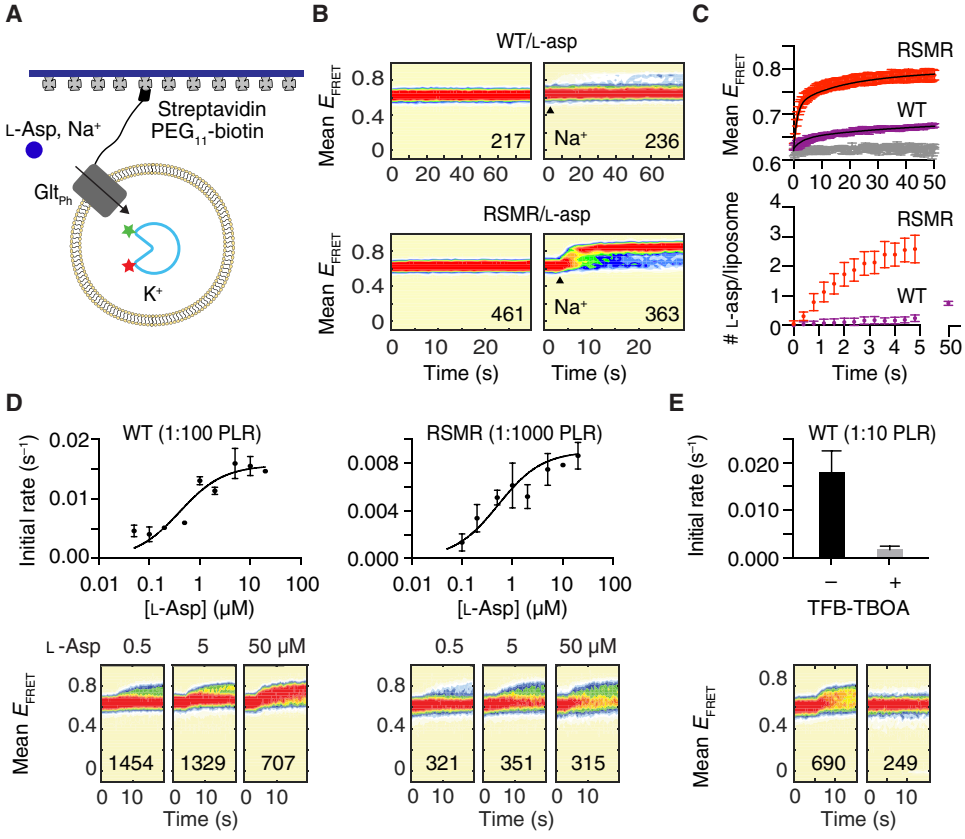

Fig. 2. Single molecule transport assay. (**A**) Cartoon representation of a proteoliposome, containing a single biotinylated Glt_{Ph} transporter and an LD555p/LD655-labeled ccPEB1a immobilized in smFRET imaging chamber via biotin-streptavidin bridge. A blue circle represents the transported sodium ions and L-asp. (**B**) Time-dependent population contour plots of ccPEB1a-Y198F inside proteoliposomes containing the WT Glt_{Ph} (top) and the RSMR mutant (bottom) in the presence of 1 μM L-asp in the external buffer either without (left) or with 200 mM NaCl (right). Black triangle marks the time of NaCl addition. (**C**) Mean FRET efficiency (purple and red, top) fitted to multiexponential functions (black lines). Controls in the absence of NaCl are shown in gray. Corresponding number of the transported L-asp molecules (bottom). (**D**) Concentration-dependent initial transport rates measured using ccPEB1-A64F/Y198F sensor and fitted to Michaelis-Menten equation. Glt_{Ph} PLR are above the panels. Representative population plots are shown below. Measurements are means and SE from three independent experiments. (**E**) Initial rate of the WT Glt_{Ph} transport in the absence (black) and presence of trifluoromethyl benzoyl amino phenyl methoxy-L-aspartic acid (TFB-TBOA) (gray). L-asp and TFB-TBOA concentrations were 0.1 and 10 μM, respectively. Representative population plots are below. Measurements are means and SD from two independent experiments.

LD555p/LD655-labeled ccPEB1a-Y198F. The remaining trajectories showed initial FRET efficiency values outside of the expected range, suggesting that the sensors either already bound their substrates during reconstitution or were denatured. Such traces were excluded from further analysis. When 1 μM L-asp was added to the vesicles in the absence of Na^+ gradient, nearly all showed stable 0.63 FRET efficiency (Fig. 2B), indicating that the sensors were properly encapsulated, and the liposomes were not leaky. When active transport was initiated upon addition of 1 μM L-asp together with 200 mM NaCl, vesicles containing the WT Glt_{Ph} or the RSMR mutant showed gradual increase in mean FRET efficiency, as L-asp was transported into the lumen and bound to ccPEB1a-Y198F (Fig. 2, B and C). As expected, proteoliposomes containing the RSMR variant exhibited a more rapid change, with a majority reaching the substrate-bound 0.85 ± 0.01 FRET efficiency state within 10 s. In contrast, only ~40% of the proteoliposomes containing WT Glt_{Ph} reached or approached 0.85 FRET efficiency state before dye photobleaching that took place with a characteristic time constant τ_{PB} of 212 ± 3 s. However, when the WT proteoliposomes were imaged 30 min after the onset of the active transport, we observed a substantial increase in the population of substrate-bound sensors exhibiting high FRET efficiency (fig. S4). These findings suggest that slow-responding WT Glt_{Ph} transporters are indeed functional but on a time scale that is slow compared with our observation window. By averaging all trajectories over the first 5 s, we estimated the mean initial rate for the WT and the RSMR mutants to be 59 ± 2 and 4.5 ± 0.2 s per turnover per transporter protomer, respectively. The rate we measured for WT Glt_{Ph} is two to three times faster than the rate measured in bulk experiments (*9*, *13*). In addition, the RSMR mutant shows a ~13-fold increase in the uptake rate compared with the fivefold increase measured in bulk (*9*, *13*). These discrepancies are not unexpected, as the suboptimal reconstitution efficiency, mixed transporter orientation, and other factors may contribute to the lower measured rates in bulk experiments.

The initial rates of the FRET efficiency increase were dependent on L-asp concentration (Fig. 2D). Consistent with previous bulk measurements (*13*), these data yielded Michaelis-Menten constants (K_m) of 400 ± 170 and 520 ± 100 nM for the WT Glt_{Ph} and the RSMR mutant, respectively. As expected, the initial rate decreased in the presence of a competitive transporter blocker, trifluoromethyl benzoyl

amino phenyl methoxy-L-aspartic acid (TFB-TBOA) (Fig. 2E). Because of the slow uptake rates of WT Glt_{Ph}, we used higher PLRs of 1:100 and 1:10 for Michaelis constant measurements and TFB-TBOA inhibition, respectively. Under these conditions, vesicles contain multiple transporters, and the obtained individual trajectories were not used for further analysis.

Static disorder of the uptake rates

When we examined individual single-molecule trajectories obtained from vesicles with PLR of 1:1000 (i.e., containing mostly single transporters), we observed a common pattern: After the application of the substrate, FRET efficiency was stable for a period of time followed by an abrupt increase (fig. S5). Such a FRET efficiency jump is, indeed, expected upon the uptake of the first L-asp (Fig. 3, A to C). The time between application of the substrate and the FRET efficiency jump, τ_{HC}, corresponds to the "first half cycle," which involves binding of L-asp to the outward-facing transporter, translocation of the transport domain into the inward-facing state, release of L-asp, and its binding to the sensor (Fig. 3, A to C, and fig. S1A). Notably, the amplitude of the jump reflects the fraction of time that the sensor spends bound to L-asp and, therefore, on the volume of the vesicle and the sensor K_d (see below). In contrast, the half-cycle time, τ_{HC}, is independent of the liposome size and is only determined by the rate of the transporter.

The Glt_{Ph} trimer is composed of protomers that function stochastically and independently of each other (*10*–*12*); therefore, any one of the three can mediate the first uptake. We analyzed trajectories originating from hundreds of WT Glt_{Ph} proteoliposomes and found that the uptake of the first L-asp occurred with vastly variable rates. Fitting the cumulative distribution of τ_{HC}'s required at least three exponentials, defining "fast," "intermediate," and "slow" transporters with corresponding τ_{HC}'*s* of ~3, 35, and 350 s (Fig. 3D and Fig. S6A). In addition, in about 60% of the vesicles, the sensors had photobleached before the entry of the first L-asp. A fraction of these are attached to the surface nonspecifically and carry no transporter, while others contain either slow or nonfunctional transporters. Notably, if a proteoliposome shows slow uptake, then that means that all three protomers of the Glt_{Ph} trimer are slow. In contrast, one fast-working protomer per trimer is enough for a proteoliposome to show fast uptake. Taking into account that there are vesicles carrying multiple trimers, we estimate that less than 15% of the transporter protomers work with fast or intermediate rates, while the majority are slow. The RSMR mutant exhibited a much narrower distribution of the first half-cycle times dominated by fast transporters with τ_{HC} of ~1 s and with a minor population of transporters with τ_{HC} of ~30 s (Fig. 3D and fig. S6B). Collectively, the data suggest that the faster uptake rates of the RSMR mutant observed in the ensemble measurements (*9*, *13*) are due to the elimination of slow transporters and a substantial increase in the population of the fast transporters.

The number of L-asp molecules that need to be transported to fully saturate the sensor depends on the size of the vesicle and on the sensor K_d. For example, ccPEB1a-Y198F is expected to be nearly saturated after ~6 molecules are transported into a vesicle with 50-nm

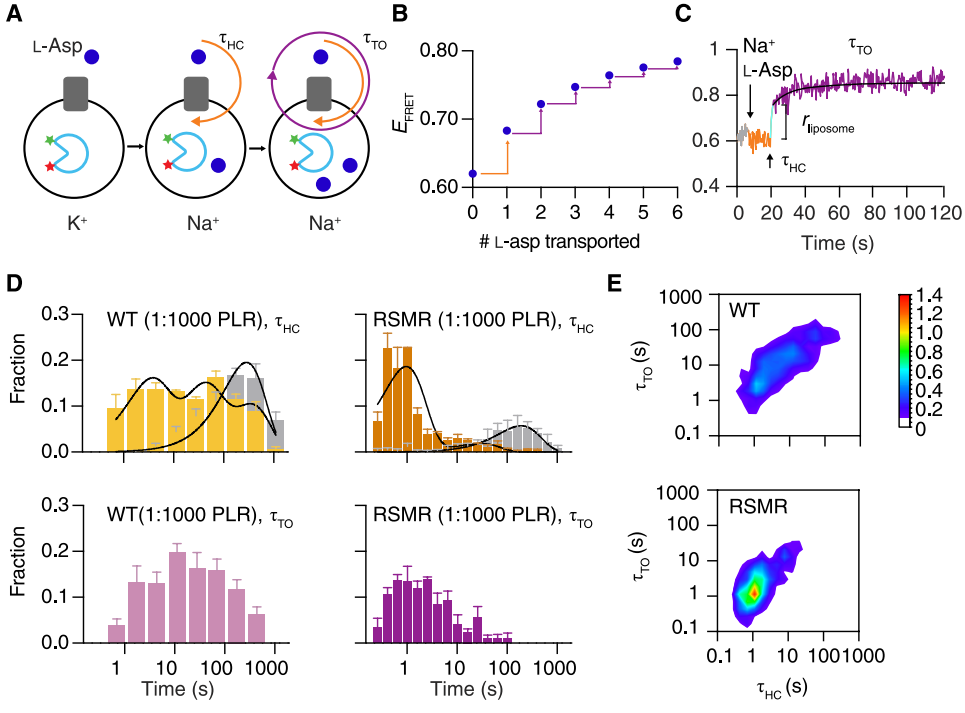

Fig. 3. Static disorder of the uptake rates. Cartoon representation of the measured time constants (**A**) and the expected stepwise FRET efficiency increases (**B**). A jump of FRET efficiency occurs after the first half cycle, τ_{HC}, following addition of NaCl to the proteoliposomes (orange). Consequent increases occur after the completion of the current cycle and the next half cycle, τ_{TO} (purple). (**C**) A representative smFRET trajectory. τ_{HC} is determined manually as the delay before the first efficiency increase, and the liposome radius is calculated from its magnitude (cyan). Consequent rise of FRET efficiency (purple) is fitted to a time-dependent binding equation (black line) to yield τ_{TO}. (**D**) Distribution of τ_{HC}'s (top) and τ_{TO}'s (bottom) for the WT (left) and the RSMR mutant (right). Gray bars correspond to ccPEB1a-Y198F molecules photobleaching before transport occurs. Data are means and SE of at least three reconstitutions comprising at least 700 and 300 molecules for τ_{HC} and τ_{TO}, respectively. Black lines are fits to the tri-, bi-, and monoexponential functions for the WT, RSMR, and photobleaching, respectively. (**E**) Population contour plots of τ_{HC} and τ_{TO} pairs. Scale bar is to the right.

radius (Fig. 3C). In some trajectories, however, the initial jump resulted in the maximal 0.85 FRET efficiency state, as would be expected for small liposomes with radius less than 25 nm, where one molecule of L-asp achieves apparent concentration >25 μM, sufficient to nearly saturate ccPEB1a-Y198F. Nonetheless, in the majority of proteoliposomes, the initial jump was smaller, and the trajectories exhibited further increases in FRET efficiency, as consecutive L-asp molecules were transported (Fig. 3, B and C and fig. S5). In such cases, we infer that experimental shot noise and instrument noise likely obscure individual transport events (fig. S5). On the basis of the amplitude of the initial FRET efficiency jump, we estimated the size of each individual vesicle. The apparent vesicle size distributions obtained were similar to those observed by negative-stain electron microscopy (fig. S7) and cryo-electron microscopy (*26*), except that the larger size vesicles were underrepresented. This is partly because negative staining method might distort liposomes (*27*) and partly because in vesicles with a radius larger than 80 nm, the FRET efficiency increases less than 10% of the maximum change after the entry of the first L-asp. For such trajectories, accurate detection of the first FRET efficiency jump is difficult, and they were not analyzed. In addition, larger vesicles are more likely to contain multiple sensors and excluded during early stages of analysis.

For further analysis, we selected traces from vesicles with radii between 25 and 80 nm that showed a gradual FRET efficiency increase following initial jump and reached or approached 0.85 FRET efficiency state. We fitted these individual FRET efficiency time courses to a time-dependent mass action binding equation, in which L-asp concentration increased linearly with a rate determined by the mean turnover time, τ_{TO}, of a given transporter (fig. S5). By analyzing simulated data generated with a range of input transport rates, we confirmed that our analysis procedure successfully recovered the τ_{HC} and τ_{TO}. Substantial deviations were observed only at very slow transport rates below 0.01 s^{-1}, where dye lifetime was not long enough to observe transport events (fig. S8).

Overall, the distributions of the turnover times, τ_{TO}'s, covered the same range as the distributions of the τ_{HC}'s (Fig. 3D). Notably, the τ_{HC} and τ_{TO} values for each individual transporter showed a nearly one-to-one correlation (Fig. 3E). Similar τ_{HC} and τ_{TO} values are consistent with an earlier hypothesis (*10*) that the outward-to-inward translocation of the substrate-bound WT transporter is rate limiting to the cycle and that the return of the empty transporter into the outward-facing state is comparatively fast (fig. S1). More notably, the close correspondence between τ_{HC} and τ_{TO} suggests that the transporters that start out fast (short τ_{HC}) continue to transport rapidly (short τ_{TO}), while those that start out slow continue to transport slowly. Particularly for the WT Glt_{Ph}, distinct transport regimes that persisted throughout the observation window were evident (Fig. 3E).

The observed kinetic heterogeneity might be due to differences in posttranslational modifications between the transporters or to differences between lipid compositions of the individual vesicles. We think that neither of these possibilities is likely because proteins expressed in *Escherichia coli* are rarely subject to posttranslational modifications and the lipid mixture used to prepare the liposomes does not contain cholesterol and therefore is unlikely to show phase separation that could lead to intervesicle differences in lipid composition (*28*). In addition, the fractions of the slow and fast transporters differ for the WT and the RSMR mutant, suggesting that differences in liposome compositions are unlikely to be the reason for the observed heterogeneity. Instead, we think that the heterogeneity reflects long-lasting, distinct activity modes due to conformational changes in the transporters that determine the transport rate and which themselves are slow, persisting over multiple turnovers. If so, we expect the transporters to switch occasionally from one mode to another. Indeed, while a majority of traces with long τ_{HC} show long τ_{TO}, ~1% shows short τ_{TO}, suggesting that these transporters have switched from a slow to a fast transport mode (fig. S9). Notably, the number of such traces is small, and the propensity to switch between modes remains ambiguous. The existence of the slow and fast transport modes is consistent with earlier smFRET studies of the conformational dynamics of the WT Glt_{Ph}, which also revealed the existence of nondynamic and dynamic periods (*9*, *10*). Furthermore, the RSMR mutant showed both a reduced propensity to sample nondynamic states in smFRET dynamics experiments (*9*) and reduced slow and intermediate transport modes in our single-molecule functional assays. It remains unknown what conformational differences underlie the existence of dynamic, fast-working and nondynamic, slow-working modes of the transporter. It is also not clear why the RSMR mutations affect their prevalence (*9*, *13*).

DISCUSSION

By using TIRF microscopy and the FRET-based L-asp sensor to establish a single-vesicle/single-transporter functional assay, we tracked single and multiple turnovers in hundreds of individual Glt_{Ph} transporters simultaneously. We deconvoluted the timing of the transport half cycles and full cycles for WT Glt_{Ph} and the gain-of-function RSMR mutant and observed broad distributions of transport rates normally masked in bulk activity measurements. In WT Glt_{Ph}, we identified at least three kinetically distinct populations with rates varying by orders of magnitude. The predominant turnover time for WT Glt_{Ph} was in the hundreds of seconds. Thus, in bulk measurements, the observed substrate uptake is mostly due to a small fraction of the fast transporters, and the apparent rates measured do not necessarily correspond to any transporters present in the population. The increased transport rate in the RSMR mutant is mostly due to the shift in the populations in favor of the fast transporters.

The distributions of the transport times for the WT Glt_{Ph} and the RSMR mutant parallel the dwell time distributions in the outward-facing state of the substrate-bound transporters obtained previously in smFRET-based conformational dynamics studies (*9*, *10*), suggesting that distinct transport rates are a consequence of distinct conformational dynamics in individual transporter protomers during the observation windows. The kinetic distinction between fast, intermediate, and slow transporters appears to persist over multiple transport cycles with infrequent switching observed both in the transport assay and in dynamics (*9*, *10*). Such mode-switching, sometimes termed "molecular memory" or static disorder of the reaction rates, has been previously observed in enzymes (*19*–*21*), ion channels (*22*–*24*), protein folding reactions (*29*–*32*), and other systems where single-molecule detection methods had been implemented. Typically, the structural basis of the rate disorder is not known. However, in one case, distinct protein folding rates, persisting over multiple folding/unfolding events, were attributed to a slow proline isomerization (*32*). While the structural underpinnings of the functional modes of Glt_{Ph} are not known, it is notable that the protein originates from a hyperthermophilic archaeon and natively functions at ca. 100°C. It seems possible that distinct low-enthalpy structural states are "frozen out" at ambient temperatures and undergo very slow interconversions.

The combination of a single-molecule approach probing conformational transitions and a single-molecule functional assay provides a powerful, and potentially generalizable, approach for accessing to the relationship between dynamics and function of transporters. Applying these approaches to a broader range of systems, and particularly to human glutamate transporters that play critical roles in the glutamatergic neurotransmission, will likely bring unknown insights into the dynamic basis of their activity and perhaps suggest previously unidentified means of their pharmacological regulation.

MATERIALS AND METHODS

DNA manipulations, expression, purification, and fluorescence labeling of PEB1a variants

Peb1a gene with a C-terminal 6xHis tag was cloned into pet21a(+) vector (GenScript) between Nde I and Bam HI sites. The single cysteine residue in the periplasmic leader sequence, Cys18, was mutated to serine. Cysteine-free construct is termed WT for brevity. Cysteine mutations Asn73Cys and Lys149Cys were introduced for labeling with donor and acceptor fluorophores. The sites were selected on the basis of the comparison of the crystal structures of the aspartate-bound PEB1a (*33*) (Protein Data Bank accession code 2V25) and of the ligand-free homolog GlnH [1WDN; (*34*)] (fig. S2A). While the apo structure of PEB1a is not known, PEB1a shares ~30% amino acid identity with GlnH, and we expect similar conformational changes upon ligand binding. Protein structures were superimposed over the larger domain (residues 1 to 100 and 196 to 233 in PEB1a), and suitable solvent-exposed residues were selected. The resulting PEB1a-N73C/K149C variant is termed ccPEB1a for brevity. Additional mutations to alter the affinity of PEB1a for L-asp were introduced using QuikChange (Agilent). The identities of all constructs were confirmed by sequencing. *E. coli* T7 Express *lysY* cells (Macrogen) were transformed with plasmids encoding PEB1a variants, and proteins were expressed and purified as described previously (*33*). Briefly, cells were grown in LB media with ampicillin (100 μg/ml) to OD (optical density) of 1 and induced with 1 mM isopropyl-β-D-1-thiogalactopyranoside (IPTG) for 3 hours at 37°C followed by 16 hours at 18°C. Cells were harvested by centrifugation for 15 min at 3326*g* at 4°C and resuspended in buffer containing 10 mM tris-HCl, pH 8.0, 2 mM EDTA, 0.5 M sucrose, and lysozyme (100 μg/ml). After 30 min on ice, the suspension was diluted 1:3 with deionized water and centrifuged for 30 min at 3578*g* at 4°C to pellet the debris. Supernatants were mixed in batch with 5 ml of Ni–NTA (nitrilotriacetic acid) resin (QIAGEN) in buffer containing 10 mM tris-HCl, pH 7.4, 200 mM NaCl, 1 mM tris(2-carboxyethyl) phosphine (TCEP). The resin was washed with the same buffer supplemented with 40 mM imidazole, and the PEB1a proteins were eluted with a 40-ml gradient from 40 to 250 mM imidazole. The eluted proteins were further purified by size exclusion chromatography (SEC) in buffer containing 10 mM tris-HCl, pH 7.4, and 200 mM NaCl using Superdex 200 10/300 GL column (GE Healthcare). Purified ccPEB1a and affinity variants were labeled with maleimide-activated LD555p and LD655 (*25*) dyes using 1:1:1 protein:LD555p:LD655 molar ratio for 1 hour at 25°C. Excess dye was removed by SEC in buffer containing 10 mM tris-HCl, pH 7.4, and 200 mM KCl. Labeled proteins were dialyzed against 4000- to 16,000-fold excess buffer to remove bound L-asp. Labeling efficiency was determined using NanoDrop 2000c (Thermo Fisher Scientific) using extinction coefficients of 18,910, 150,000, and 250,000 M^{-1} cm^{-1} for protein at 280 nm, LD555p at 550 nm, and LD655 at 650 nm. Typical labeling efficiency was 60% for LD555p and 100% for LD655. Proteins were concentrated to 3 μM using 10-kDa cutoff concentrators (EMD Millipore) and stored in liquid nitrogen until further use.

Labeling specificity was confirmed by incubating WT PEB1a and ccPEB1a with LD555p/LD655 dyes at 1:1:1 molar ratio for 5 to 80 min, after which the reaction was quenched using 0.7 M 2-mercaptoethanol (BME). Samples were analyzed by SDS–polyacrylamide gel electrophoresis and visualized using ChemiDoc-MP Imaging System (Bio-Rad). For LD555p, the fluorescence was excited at 520 to 545 nm, and emission was detected using a 500/50 band-pass filter. For LD655, the fluorescence was excited at 625 to 650 nm, and emission was detected using a 602/50 band-pass filter.

Bulk fluorometer measurements of L-asp binding to ccPEB1a variants

FRET efficiency changes of LD555p/LD655-labeled ccPEB1a variants in response to L-asp binding were measured using a bulk PTI QuantaMaster 400 fluorometer (Horiba). Protein was diluted to a final concentration of 20 nM in 1.5 ml of buffer containing 50 mM Hepes/tris, pH 7.4, and 200 mM KCl. Fluorescence was excited at 532 nm, and emission was recorded between 550 and 750 nm before and after the addition of L-asp aliquots. To obtain L-asp binding isotherms, LD555p was excited at 532 nm and LD655 emission at 672 nm was measured continuously with 0.2-Hz rate. Samples were incubated at 25°C with continuous stirring, L-asp aliquots were added, and changes of LD655 fluorescence were recorded after 60 s of equilibration. Raw fluorescence signal was corrected for dilution and normalized to yield percent change. To obtain K_d, the data were fitted in Prism (GraphPad) to the following equation

$$Y = a + b\log(X) + X^{*}\frac{100}{(X + K_d)} \quad (1)$$

where X = [L-asp] and parameters a and b account for a gradual decrease in the overall fluorescence observed over the duration of the experiment, which might be due to fluorophore photobleaching. For presentation purposes, the data were plotted as a fraction of the bound protein.

Glt_{Ph} purification and labeling

The Asn378Cys mutant of a cysteine-less variant of Glt_{Ph} and the RSMR mutant with a C-terminal thrombin cleavage site and 8xHis tag were expressed in *E. coli* and purified as described previously (*9*). Briefly, crude cell membranes were homogenized in buffer containing 50 mM Hepes/tris, pH 7.4, 200 mM NaCl, 1 mM L-asp, and 1 mM TCEP and solubilized by the addition of 40 mM *N*-dodecyl β-D-maltopyranoside (DDM) for 1 hour at 4°C. Following centrifugation to remove insoluble material, the transporters were purified by immobilized Ni-NTA chromatography in the same buffer supplemented with 1 mM DDM and eluted in the presence of 250 mM imidazole. The His tag was cleaved by thrombin, and the protein was further purified by SEC in 50 mM Hepes/tris, pH 7.4, 200 mM NaCl, 0.1 mM L-asp, and 1 mM DDM. Glt_{Ph} was labeled with maleimide-activated biotin-PEG_{11} (EZ-Link, Thermo Fisher Scientific) in the presence of *N*-ethylmaleimide (NEM) at a molar ratio of 1:2:4 (protein:biotin-PEG_{11}:NEM) for 1 hour at 25°C. Excess reagents were removed by SEC. Protein samples were concentrated to 10 mg/ml using 100-kDa cutoff concentrators and reconstituted immediately.

To determine the stoichiometry of Glt_{Ph} per liposome, protein was purified as described above and labeled with LD555p at a molar ratio of 1:6 (protein:LD555p) for 1 hour at 25°C. Excess dye was removed by SEC. Labeling efficiency was determined to be ~96% using NanoDrop 2000c (Thermo Fisher Scientific) using extinction coefficients of 57,400 M^{-1} cm^{-1} at 280 nm and 150,000 M^{-1} cm^{-1} at 550 nm for protein and LD555p, respectively.

Glt_{Ph} reconstitution into liposomes and PEB1a encapsulation

Labeled WT Glt_{Ph} and the RSMR mutant were reconstituted into liposomes, as previously described (*9*). Briefly, liposomes were prepared from 3:1 (w/w) mixture of *E. coli* polar lipid extract (Avanti Polar Lipids Inc.) and egg phosphatidylcholine in buffer A containing 50 mM Hepes/tris, pH7.4, and 200 mM KCl by extrusion through 100-nm filters (Whatman Nuclepore) using syringe extruder (Avanti Polar Lipids Inc.). Liposomes were destabilized by the addition of Triton X-100 at 1:2 (w/w) detergent-to-lipid ratio. Glt_{Ph} was added to destabilized liposomes at 1:1000 (w/w) PLR or at other PLRs, as indicated in the text and figures and incubated at 25°C for 30 min. Detergent was removed by six rounds of incubation with Bio-Beads (Bio-Rad) at 80 mg/ml. Liposomes were loaded with buffer A by three freeze/thaw cycles and concentrated to 25 mg/ml, ~100 μl. PEB1a variants were added to final concentrations of 0.6 μM and encapsulated by two freeze-thaw cycles. To remove excess PEB1a in the external solution, the liposomes were centrifuged for 1 hour at 49,192*g* at 4°C and the supernatants were discarded. Liposomes were suspended in 100 μl of buffer A and extruded through 100-nm filters 10 times.

smFRET experiments

All experiments were performed using a home-built prism-based TIRF microscope constructed around a Nikon Eclipse Ti inverted microscope body (*17*). The samples were illuminated with a 532-nm laser (Laser Quantum), and LD555p and LD655 fluorescence signals were separated using a T635lpxr dichroic filter (Chroma) mounted in a MultiCam apparatus (Cairn). Imaging data were acquired using home-written acquisition software and scientific complementary metal-oxide semiconductor (sCMOS) cameras (Hamamatsu). Before the experiments, microfluidic imaging chambers were passivated with biotin-PEG and coated with streptavidin, as previously described (*9*). Briefly, after passivation, the microfluidic channel was incubated with buffer A supplemented with 0.8 μM streptavidin (Invitrogen) for 10 min and rinsed thoroughly.

To measure binding characteristics, LD555p/LD655-labeled PEB1a variants were immobilized by incubating the channel consecutively with biotin-tris-NTA-Ni^{2+} (*35*, *36*) and 10 nM PEB1a with 6xHis tag for 5 min each. Unbound reagents were washed away with 1 ml of buffer A following each incubation. For transport assay measurements, proteoliposomes were immobilized by incubating 10 nM samples in buffer A in channels for 5 min followed by 1 ml of wash to remove unbound vesicles. All buffers were supplemented with oxygen-scavenging system composed of 2 mM protocatechuic acid (PCA) and 50 nM protocatechuate-3,4-dioxygenase (PCD), as described previously (*37*). Typically, the smFRET recordings were carried out with 5- to 400-ms integration time using 500- to 20-mW laser power. Fluorescence emission trajectories were extracted and selected for further analysis using Spartan software (*17*). Only those trajectories that lasted longer than 15 frames with a signal-to-noise ratio larger than 8 were selected for further analysis. Fluorescence signals were corrected for spectral cross-talk. FRET efficiencies were calculated as $E_{FRET} = I_{LD655}/(I_{LD555p} + I_{LD655})$. Trajectories corresponding to multiple sensors as indicated by multiple LD555p and/or LD655 photobleaching events were discarded. We also discarded trajectories that showed initial values of FRET efficiency either below 0.4 or above 0.7, which correspond to sensors that are already bound to their substrate and sensors that are denatured.

Characterization of L-asp binding to PEB1a using smFRET

To measure L-asp binding, LD555p/LD655-labeled ccPEB1A variants were imaged at 100-ms time resolution, 50-mW laser power in buffer A supplemented with 0 to 100 μM L-asp. The mean FRET efficiencies for all molecules were plotted as functions of L-asp concentrations and fitted to a single-site binding equation in Prism. For presentation purposes, binding isotherms were plotted as fractions of the bound protein. To determine L-asp binding and unbinding rate constants, k_{on} and k_{off}, respectively, smFRET trajectories were idealized in Spartan using segmental *k*-means algorithm (*38*). A three-state model was used with FRET efficiency states of 0.65, 0.87, and 0 corresponding to ligand-free, ligand-bound, and photobleached states, respectively. The mean values of the ligand-free and ligand-bound FRET efficiencies were based on the fits of population histograms obtained in the absence of L-asp and in the presence of saturating 1 μM L-asp, respectively. The unbinding k_{off} rate was determined by fitting the survival plots of the ~0.87 FRET efficiency state at 1 nM L-asp to a single exponential decay function. The binding rate k_{on} was calculated on the basis of the equation $k_{on} = k_{off}/K_d$ and using estimated K_d of 79 nM.

Glt_{Ph} and PEB1a stoichiometry in liposomes

We estimated the expected number of the transporters per proteoliposomes as a function of PLR assuming uniform 100-nm-size vesicles and Poisson distribution, as described previously (*39*). Briefly, the number of lipid molecules per vesicle *L* is

$$L = \frac{4\pi r^2 + 4\pi (r-d)^2}{s} \quad (2)$$

where *r* is the radius of the liposomes, *d* is the bilayer thickness, and *s* is the surface area of the lipid headgroups. The number of lipid molecules in a given preparation, *l*, is

$$l = \frac{X \times 10^{-3} N_A}{\mathrm{MW\ (lipid)}} \quad (3)$$

where *X* is the amount of lipids used to form liposomes in milligram, N_A is Avogadro's constant, and MW (lipid) is the mean molecular weight of the lipid mixture used for reconstitution. The number of proteins used in reconstitution, *P*, is

$$P = \frac{X \times 10^{-3} N_A \times \mathrm{PLR}}{\mathrm{MW(protein)}} \quad (4)$$

If all proteins were successfully reconstituted, the average number of proteins per liposome, μ, would be

$$\mu = \frac{P \times l}{L} \quad (5)$$

Proteins were reconstituted into liposomes prepared from *E. coli* polar extract whose major components are PE (67%) and phosphatidylglycerol (PG) (23%). In our calculations, bilayer thickness, *d*,

and surface area, *s*, are assumed to be 36 Å and 60 Å^2, respectively, based on values obtained in molecular dynamics simulations for PE:PG bilayer (*40*). These values yield an estimate of ~100,000 lipids per vesicle with 100-nm diameter. Using 731.5 Da as an average molecular weight of lipids and 134,000 Da for the molecular weight of Glt_{Ph} trimer, we estimate that for 0.5 trimers per vesicle, there are ~5.4 trimers per 10^6 lipids.

The probability of observing a given number of transporters, λ per liposome is defined by Poisson distribution

$$p(\lambda) = \frac{\mu^{\lambda}}{\lambda! \times (e^{\mu})} \quad (6)$$

The PLR of 1:1000 used during reconstitution of Glt_{Ph} is expected to yield 61% empty liposomes. Of the 39% vesicles that contain transporters, 77% are expected to have one, 19% to have two, and 4% to have more than two transporters. To empirically determine the transporter number in liposomes, LD555p-labeled transporters were reconstituted into liposomes as usual, except that the liposomes were supplemented with 1% (w/w) biotin-PE (Avanti Polar Lipids Inc.). Liposomes were then imaged by smFRET, and the number of the photobleaching events per liposome was quantified. To quantify the stoichiometry of PEB1a encapsulation, the number of photobleaching steps for LD555p and LD655 dyes in trajectories collected for transport assay were counted. We used a PLR of 1:100 and 1:10 for K_m and TFB-TBOA inhibition measurements of WT Glt_{Ph}, respectively. On the basis of the calculations above, at a PLR of 1:100, almost all of the vesicles are expected to have at least 1 transporter with ~74% of them containing more than 3 transporters, whereas at a PLR of 1:10, all of the vesicles contain at least 25 transporters.

smFRET-based transport assay

In all transport experiments, we used the ccPEB1a-Y198F L-asp sensor unless otherwise stated. For each preparation of immobilized proteoliposomes, we first tested for vesicle leakage in buffer containing 50 mM Hepes/tris, pH 7.4, 200 mM KCl, and 1 μM L-asp. Approximately 4% of ccPEB1a molecules showed a FRET efficiency change, suggesting that either they were not properly encapsulated or the liposomes were leaky. Transport was initiated by replacing the buffer with 50 mM Hepes/tris, pH7.4, 200 mM NaCl, and 1 μM L-Asp, unless otherwise stated, approximately 3 s after the start of imaging using a rapid perfusion system. Data were collected with time resolutions of 400 and 200 ms for the WT Glt_{Ph} and the RSMR mutant, respectively, using corresponding laser powers of 20 and 50 mW, measured immediately downstream of the laser head. Each individual trajectory that showed initial FRET efficiency between 0.4 and 0.7 and stable mean total fluorescence intensity was analyzed manually for the timing of the first transport event. Liposome size and transport turnover rates were extracted from each trace using a MATLAB script (see below). Histograms of τ_{HC} and τ_{TO} were fitted to exponential distribution (*41*), and the histograms of the liposome sizes were generated using Prism.

To measure K_m values, WT Glt_{Ph} and RSMR mutant were reconstituted at 1:100 and 1:1000 PLR, respectively, and the proteoliposomes were loaded with ccPEB1a-Y198F/A64F, which has 21 μM affinity for L-asp. The proteoliposomes were imaged as usual in the presence of variable L-asp concentrations. The mean FRET efficiency changes over the first 5 s after active transport initiation were fitted by linear regression to obtain initial uptake rates. Data were fitted to Michaelis-Menten equation with a Hill coefficient of one.

To measure inhibition using TFB-TBOA, WT Glt_{Ph} proteoliposomes were reconstituted at 1:10 PLR with encapsulated ccPEB1a-Y198F/A64F and imaged at 200-ms time resolution. Active transport was initiated by perfusion of 200 mM NaCl, 100 nM L-asp with or without 30 s before incubation with 10 μM TFB-TBOA in 200 mM NaCl. The mean FRET efficiency changes over the first 5 s after active transport initiation were fitted by linear regression to obtain the initial rates.

To measure nonspecific binding, biotinylated WT Glt_{Ph} was reconstituted at 1:1000 PLR and proteoliposomes were loaded with LD555p/LD655-labeled ccPEB1a-Y198F. Sample was immobilized on the surface of single molecule chambers with or without streptavidin coating, using similar concentrations and volumes. Trajectories from these datasets were selected using the same criteria. The number of molecules in the datasets acquired in the absence of streptavidin constituted ~26% of those that were acquired with streptavidin. Notably, of these trajectories, only 15% showed FRET efficiency changes suggestive of L-asp uptake.

Analysis of the transport smFRET trajectories

Each trajectory was analyzed to extract τ_{HC} and τ_{TO} (see Static disorder of the uptake rates in the Results section). τ_{HC} was determined manually from the delay between the addition of L-asp and NaCl and the first abrupt increase in FRET efficiency. Because the exact time at which the buffer replacement occurs within the imaging field is not known, we used the time of the earliest jump in FRET efficiency (minimum τ_{HC}) observed for any trace in the dataset as an approximation. τ_{TO} was determined from fitting the tail rise in each trace following the initial FRET efficiency jump to a time-dependent binding equation, where we considered L-asp flux into the liposomes with the rate determined by τ_{TO}. To enable such fits, it is essential to determine the apparent concentration of L-asp as a function of the number of molecules entering the proteoliposome. For this, it is necessary to estimate the volume of each proteoliposome, which varies substantially in the population. Toward this end, we note that the magnitude of the FRET efficiency increase upon uptake of the first molecule of L-asp is dependent on the liposome size and the K_d of the encapsulated ccPEB1a sensor, which for ccPEB1a-Y198F was 5.6 ± 0.1 μM based on bulk fluorometer measurements. Normalized FRET efficiency increase, J_1, is defined as

$$J_1 = \frac{FRET_{jump} - FRET_{unbound}}{FRET_{bound} - FRET_{unbound}} \quad (7)$$

where $FRET_{jump}$ is determined by averaging the first two frames following the jump (Fig. 3). The value of J_1 reflects the fraction of the time, $F_{B,t,1}$, that PEB1a spends bound to L-asp, which depends on PEB1a K_d for L-asp

$$F_{B,t,1} = J_1 = \frac{\left(([L_T]+[S_T]+K_d) - \sqrt{([L_T]+[S_T]+K_d)^2 - 4[L_T][S_T]}\right)}{2[S_T]} \quad (8)$$

where $[L_T]$ is the total concentration of L-asp in the liposome and $[S_T]$ is the total concentration of ccPEB1a. When the first L-asp enters the liposome

$$[L_T] = [S_T] = \frac{3 \times 1000}{4 N_A \pi r^3} \quad (9)$$

where r is the radius of the vesicle in meters. Equation (8) can be simplified

$$J_1 = \frac{\left((2[L_T]+K_d)-\sqrt{(2[L_T]+K_d)^2-4[L_T]^2}\right)}{2[L_T]} \quad (10)$$

Solving for $[L_T]$

$$[L_T] = \frac{K_d J_1}{(1-J_1)^2} \quad (11)$$

Therefore, r in meters can be calculated from the value of J_1

$$r = \sqrt[3]{\frac{3000(1-J_1)^2}{4\pi N_A K_d J_1}} \quad (12)$$

Once the liposome size is determined, the tail rise of FRET efficiency following the initial jump, $J(t)$, corresponding to the fraction of time that ccPEB1a is bound to L-asp can be fitted to the equation

$$J(t) = F_{B,t}(t) = \frac{\left(([L_T](t)+[S_T]+K_d)-\sqrt{([L_T](t)+[S_T]+K_d)^2-4[L_T](t)[S_T]}\right)}{2[S_T]} \quad (13)$$

where $[L_T](t)$ is the time-dependent concentration of L-asp determined by the transport rate, $1/\tau_{TO}$

$$[L_T](t) = \frac{3000\left(1+\frac{t}{\tau_{TO}}\right)}{4\pi r^3 N_A} \quad (14)$$

where t is time since the uptake of the first L-asp molecule. Trajectories with fits that had R^2 values below 0.2 indicating poor fits were excluded from further analysis. These included trajectories corresponding to liposomes with radii smaller than 25 nm where the sensor was saturated upon the uptake of the first L-asp, trajectories with high noise levels comparable to J_1, and trajectories with τ_{PB} shorter than $2x\tau_{TO}$. For the WT Glt_{Ph} trajectories with τ_{PB} shorter than $2x\tau_{TO}$, we used the length of $\tau_{PB} - \tau_{HC}$/number of steps as an estimate of the lower boundary of τ_{TO} in distributions of turnover time.

Distribution histograms of τ_{HC} and τ_{TO} were fitted to an exponential probability distribution function (PDF) (*41*) using the following equation

$$\mathrm{PDF}(x) = \ln(10) \times 10^{(x-x0)} \times e^{-10^{(x-x0)}} \quad (15)$$

where $x = \log_{10}(t)$ and $x0$ is $\log_{10}(\tau_{HC})$ or $\log_{10}(\tau_{TO})$. Cumulative survival plots were fitted to the sums of exponentials.

To convert the mean FRET efficiency evolution $<J(t)>$ obtained by averaging hundreds of individual smFRET traces to mean number of L-asp molecules transported into vesicles, we rearranged Eq. (13)

$$\langle [L_T](t)\rangle = \frac{\langle J(t)\rangle(\langle [S_T]\rangle - \langle J(t)\rangle\langle [S_T]\rangle + K_d)}{1-\langle J(t)\rangle} \quad (16)$$

Assuming that all liposomes are uniformly sized with radius r = 50 nm, we obtain the mean number of molecules transported per vesicle, $<\eta(t)>$, equivalent to the mean number of L-asp transported per Glt_{Ph} trimer

$$\langle \eta(t)\rangle = \frac{4}{3000}\pi r^3 N_A \langle [L_T](t)\rangle \quad (17)$$

Simulating smFRET trajectories

Using Spartan, we simulated single-molecule FRET trajectories over a range of transport rates ($1/\tau_{HC}$ and $1/\tau_{TO}$) to determine whether our procedure of manually determining τ_{HC} and fitting tail rise of the FRET trajectories to obtain τ_{TO} yielded accurate transport rates. A six-state model was used with FRET efficiency states corresponding to the efficiencies of ccPEB1a-Y198F in the presence of zero to five molecules of L-asp in the vesicle. The efficiencies were calculated using Eq. 13 after converting the number of molecules to concentration using a liposome radius of 50 nm. Poisson shot noise was added and signal–to–background noise ratio was adjusted to best mimic the experimental data. Mean total photon count was set to 500 and integration time to 400 ms. The trajectories were truncated at the end of 2000 frames. Donor and acceptor fluorophores were set to photobleach exponentially with characteristic lifetimes, τ_{PB}, of 300 and 200 s, respectively. Eleven datasets each comprising 100 trajectories were simulated with transport rates between 0.004 and 0.5 L-asp molecules per second (with identical values set for τ_{HC} and τ_{TO}). Datasets and the extracted values of τ_{HC} and τ_{TO} were analyzed exactly as for experimental data. Correlation plots of the input and output τ_{HC} and τ_{TO} values were generated in Prism.

SUPPLEMENTARY MATERIALS

Supplementary material for this article is available at http://advances.sciencemag.org/cgi/content/full/6/22/eaaz1949/DC1

View/request a protocol for this paper from *Bio-protocol*.

REFERENCES AND NOTES

1. D. Drew, O. Boudker, Shared molecular mechanisms of membrane transporters. *Annu. Rev. Biochem.* **85**, 543–572 (2016).
2. O. P. Hamill, A. Marty, E. Neher, B. Sakmann, F. J. Sigworth, Improved patch-clamp techniques for high-resolution current recording from cells and cell-free membrane patches. *Pflugers Arch.* **391**, 85–100 (1981).
3. E. Neher, B. Sakmann, Single-channel currents recorded from membrane of denervated frog muscle fibres. *Nature* **260**, 799–802 (1976).
4. E. E. Weatherill, M. I. Wallace, Combining single-molecule imaging and single-channel electrophysiology. *J. Mol. Biol.* **427**, 146–157 (2015).
5. D. Yernool, O. Boudker, Y. Jin, E. Gouaux, Structure of a glutamate transporter homologue from *Pyrococcus horikoshii*. *Nature* **431**, 811–818 (2004).
6. O. Boudker, R. M. Ryan, D. Yernool, K. Shimamoto, E. Gouaux, Coupling substrate and ion binding to extracellular gate of a sodium-dependent aspartate transporter. *Nature* **445**, 387–393 (2007).
7. N. Reyes, C. Ginter, O. Boudker, Transport mechanism of a bacterial homologue of glutamate transporters. *Nature* **462**, 880–885 (2009).
8. M. Groeneveld, D.-J. Slotboom, Na^+:aspartate coupling stoichiometry in the glutamate transporter homologue Glt(Ph). *Biochemistry* **49**, 3511–3513 (2010).
9. N. Akyuz, E. R. Georgieva, Z. Zhou, S. Stolzenberg, M. A. Cuendet, G. Khelashvili, R. B. Altman, D. S. Terry, J. H. Freed, H. Weinstein, O. Boudker, S. C. Blanchard, Transport domain unlocking sets the uptake rate of an aspartate transporter. *Nature* **518**, 68–73 (2015).
10. N. Akyuz, R. B. Altman, S. C. Blanchard, O. Boudker, Transport dynamics in a glutamate transporter homologue. *Nature* **502**, 114–118 (2013).
11. Y. Ruan, A. Miyagi, X. Wang, M. Chami, O. Boudker, S. Scheuring, Direct visualization of glutamate transporter elevator mechanism by high-speed AFM. *Proc. Natl. Acad. Sci. U.S.A.* **114**, 1584–1588 (2017).
12. G. B. Erkens, I. Hänelt, J. M. Goudsmits, D. J. Slotboom, A. M. van Oijen, Unsynchronised subunit motion in single trimeric sodium-coupled aspartate transporters. *Nature* **502**, 119–123 (2013).
13. R. M. Ryan, N. C. Kortt, T. Sirivanta, R. J. Vandenberg, The position of an arginine residue influences substrate affinity and K^+ coupling in the human glutamate transporter, EAAT1. *J. Neurochem.* **114**, 565–575 (2010).
14. M. Del. Rocio Leon-Kempis, E. Guccione, F. Mulholland, M. P. Williamson, D. J. Kelly, The *Campylobacter jejuni* PEB1a adhesin is an aspartate/glutamate-binding protein of an ABC

transporter essential for microaerobic growth on dicarboxylic amino acids. *Mol. Microbiol.* **60**, 1262–1275 (2006).
15. R. M. de Lorimier, J. J. Smith, M. A. Dwyer, L. L. Looger, K. M. Sali, C. D. Paavola, S. S. Rizk, S. Sadigov, D. W. Conrad, L. Loew, H. W. Hellinga, Construction of a fluorescent biosensor family. *Protein Sci.* **11**, 2655–2675 (2002).
16. D. Axelrod, Cell-substrate contacts illuminated by total internal reflection fluorescence. *J. Cell Biol.* **89**, 141–145 (1981).
17. M. F. Juette, D. S. Terry, M. R. Wasserman, R. B. Altman, Z. Zhou, H. Zhao, S. C. Blanchard, Single-molecule imaging of non-equilibrium molecular ensembles on the millisecond timescale. *Nat. Methods* **13**, 341–344 (2016).
18. G. A. Fitzgerald, D. S. Terry, A. L. Warren, M. Quick, J. A. Javitch, S. C. Blanchard, Quantifying secondary transport at single-molecule resolution. *Nature* **575**, 528–534 (2019).
19. H. Yang, G. Luo, P. Karnchanaphanurach, T.-M. Louie, I. Rech, S. Cova, L. Xun, X. S. Xie, Protein conformational dynamics probed by single-molecule electron transfer. *Science* **302**, 262–266 (2003).
20. B. P. English, W. Min, A. M. van Oijen, K. T. Lee, G. Luo, H. Sun, B. J. Cherayil, S. C. Kou, X. S. Xie, Ever-fluctuating single enzyme molecules: Michaelis-Menten equation revisited. *Nat. Chem. Biol.* **2**, 87–94 (2006).
21. X. Zhuang, H. Kim, M. J. Pereira, H. P. Babcock, N. G. Walter, S. Chu, Correlating structural dynamics and function in single ribozyme molecules. *Science* **296**, 1473–1476 (2002).
22. A. L. Blatz, K. L. Magleby, Quantitative description of three modes of activity of fast chloride channels from rat skeletal muscle. *J. Physiol.* **378**, 141–174 (1986).
23. O. B. Mcmanus, K. L. Magleby, Kinetic states and modes of single large-conductance calcium-activated potassium channels in cultured rat skeletal muscle. *J. Physiol.* **402**, 79–120 (1988).
24. A. Auerbach, C. J. Lingle, Heterogeneous kinetic properties of acetylcholine receptor channels in Xenopus myocytes. *J. Physiol.* **378**, 119–140 (1986).
25. R. B. Altman, Q. Zheng, Z. Zhou, D. S. Terry, J. D. Warren, S. C. Blanchard, Enhanced photostability of cyanine fluorophores across the visible spectrum. *Nat. Methods* **9**, 428–429 (2012).
26. L. Cliff, R. Chadda, J. L. Robertson, Occupancy distributions of membrane proteins in heterogeneous liposome populations. *Biochim. Biophys. Acta Biomembr.* **1862**, 183033 (2020).
27. U. Baxa, Imaging of liposomes by transmission electron microscopy. *Methods Mol. Biol.* **1682**, 73–88 (2018).
28. F. M. Goñi, A. Alonso, L. A. Bagatolli, R. E. Brown, D. Marsh, M. Prieto, J. L. Thewalt, Phase diagrams of lipid mixtures relevant to the study of membrane rafts. *Biochim. Biophys. Acta* **1781**, 665–684 (2008).
29. J. F. Brandts, H. R. Halvorson, M. Brennan, Consideration of the Possibility that the slow step in protein denaturation reactions is due to cis-trans isomerism of proline residues. *Biochemistry* **14**, 4953–4963 (1975).
30. P. J. Hagerman, R. L. Baldwin, A quantitative treatment of the kinetics of the folding transition of ribonuclease A. *Biochemistry* **15**, 1462–1473 (1976).
31. K. Kuwajima, F. X. Schmid, Experimental studies of folding kinetics and structural dynamics of small proteins. *Adv. Biophys.* **18**, 43–74 (1984).
32. L. N. Lin, H. Hasumi, J. F. Brandts, Catalysis of proline isomerization during protein-folding reactions. *Biochim. Biophys. Acta* **956**, 256–266 (1988).
33. A. Muller, M. del R. León-Kempis, E. Dodson, K. S. Wilson, A. J. Wilkinson, D. J. Kelly, A bacterial virulence factor with a dual role as an adhesin and a solute-binding protein: The crystal structure at 1.5 Å resolution of the PEB1a protein from the food-borne human pathogen *Campylobacter jejuni*. *J. Mol. Biol.* **372**, 160–171 (2007).
34. C. D. Hsiao, Y. J. Sun, J. Rose, B. C. Wang, The crystal structure of glutamine-binding protein from *Escherichia coli*. *J. Mol. Biol.* **262**, 225–242 (1996).
35. R. Roy, S. Hohng, T. Ha, A practical guide to single-molecule FRET. *Nat. Methods* **5**, 507–516 (2008).
36. A. Reichel, D. Schaible, N. Al Furoukh, M. Cohen, G. Schreiber, J. Piehler, Noncovalent, site-specific biotinylation of histidine-tagged proteins. *Anal. Chem.* **79**, 8590–8600 (2007).
37. C. E. Aitken, R. A. Marshall, J. D. Puglisi, An oxygen scavenging system for improvement of dye stability in single-molecule fluorescence experiments. *Biophys. J.* **94**, 1826–1835 (2008).
38. F. Qin, Restoration of single-channel currents using the segmental k-means method based on hidden Markov modeling. *Biophys. J.* **86**, 1488–1501 (2004).
39. M. Walden, A. Accardi, F. Wu, C. Xu, C. Williams, C. Miller, Uncoupling and turnover in a Cl-/H^+ exchange transporter. *J. Gen. Physiol.* **129**, 317–329 (2007).
40. K. Murzyn, T. Róg, M. Pasenkiewicz-Gierula, Phosphatidylethanolamine-phosphatidylglycerol bilayer as a model of the inner bacterial membrane. *Biophys. J.* **88**, 1091–1103 (2005).
41. F. J. Sigworth, S. M. Sine, Data transformations for improved display and fitting of single-channel dwell time histograms. *Biophys. J.* **52**, 1047–1054 (1987).
42. Y. J. Sun, J. Rose, B. C. Wang, C. D. Hsiao, The structure of glutamine-binding protein complexed with glutamine at 1.94 Å resolution: Comparisons with other amino acid binding proteins. *J. Mol. Biol.* **278**, 219–229 (1998).

Acknowledgments: We thank R. Altman for the preparation of smFRET chambers; C. Miller, D. Stamou, R. Hite, and J. Chodera for the helpful discussions. **Funding:** NINDS R37NS085318 to O.B. and S.C.B., and AHA 19PRE34380215 to D.C. This project has received funding from the European Union's Horizon 2020 research and innovation program under the Maire Sklodowska-Curie grant agreement MEMDYN no. 660083 (G.H.M.H.). **Author contributions:** Conceptualization: O.B., S.C.B., D.C., D.T., and G.F. Data acquisition: D.C., X.W., and C.H. Analysis: O.B., D.C., G.H.M.H., and C.H. Fluorophore synthesis: Z.Z. Manuscript writing: O.B., D.C., G.H.M.H., S.C.B., D.T., and G.F. **Competing interests:** The authors declare that they have no competing interests. **Data and materials availability:** All data needed to evaluate the conclusions in the paper are present in the paper and/or the Supplementary Materials. Additional data related to this paper may be requested from the authors.

Submitted 20 August 2019
Accepted 26 March 2020
Published 29 May 2020
10.1126/sciadv.aaz1949

Citation: D. Ciftci, G. H. M. Huysmans, X. Wang, C. He, D. Terry, Z. Zhou, G. Fitzgerald, S. C. Blanchard, O. Boudker, Single-molecule transport kinetics of a glutamate transporter homolog shows static disorder. *Sci. Adv.* **6**, eaaz1949 (2020).